Research Square

Preprints are preliminary reports that have not undergone peer review.
They should not be considered conclusive, used to inform clinical practice,
or referenced by the media as validated information.

Terahertz Spectroelectrochemistry (THz-SEC) Enables Bias Resolved THz Spectroscopy (BRTS) to Probe Trap State Occupancy and Energetics

Kendra Hamilton
University of North Texas
Mari Salinas
University of North Texas
Jens Neu
jens.neu@unt.edu
University of North Texas

Research Article

Keywords:

Posted Date: November 27th, 2026

DOI: https://doi.org/10.21203/rs.3.rs-11776530/v1

License: This work is licensed under a Creative Commons Attribution 4.0 International License.
Read Full License

Additional Declarations: No competing interests reported.

Terahertz Spectroelectrochemistry (THz-SEC) Enables Bias Resolved THz Spectroscopy (BRTS) to Probe Trap State Occupancy and Energetics

Kendra Hamilton[1*], Mari Salinas[1] and Jens Neu[1,2*]

[1]Physics Department, University of North Texas, 210 Ave A, Denton, 76201, Texas, United States of America.
[2]Center for Microelectronics in Extreme Environments, University of North Texas, 3940 N. Elm Street, Denton, 76207, Texas, United States of America.

*Corresponding author(s). E-mail(s): KendraHamilton2@my.unt.edu; Jens.Neu@unt.edu;
Contributing authors: MariSalinas@my.unt.edu;

Abstract

Terahertz spectroelectrochemistry (THz-SEC) provides control over the Fermi level while monitoring the THz transmission through a material. We developed a new THz and optically transparent electrochemical cell, with minimized liquid pathway to ensure high THz transmission. We demonstrated THz cyclic voltammetry (TCV), which provides insight into trap state energetics. Further, we measured full time-domain spectroscopy traces under controlled Fermi level conditions. These bias resolved THz spectroscopy (BRTS) measurements allow us to extract conductivity values under fuel cell operating conditions. We demonstrated these new techniques on model metal-oxide semiconductors: $\boldsymbol{TiO_2}$ and $\boldsymbol{SnO_2}$. Even in such a well studied system, THz-SEC provides previously uncharacterized insight into the trap state energetics. In $\boldsymbol{SnO_2}$, a distinct conductivity onset near -0.25 V versus Ag/AgCl followed by continued increases in conductivity at more negative potentials reveals the progressive trap state ionization and occupation of conduction band states. We further developed a method for extracting a quantitative description of the bias-induced conductivity in $\boldsymbol{SnO_2}$. These results represent the first direct measurement of THz conductivity in operando, under applied bias and within the electrolyte environment of a representative photoelectrochemical cell. The extracted bias-induced conductivity is well-represented by the Drude-Smith model and allows us to directly quantify the bias-dependent carrier density.

Keywords: Spectroscopy, Electrochemistry, Semiconductors, Fuel Cells

1 Introduction

Photoelectrochemical (PEC) cells convert solar energy into chemical fuels using the photoexcitation of semiconductor materials to drive nonspontaneous chemical reactions. PEC system designs consisting of a metal-oxide semiconductor sensitized by a visible light absorber and/or a photocatalyst have been widely investigated for applications in solar-driven water splitting [1][2]. In these systems, the semiconductor serves as a pathway for charge transport. Excited electrons in the sensitizer are injected into the semiconductor conduction band, where they must be efficiently extracted and transported through the electrode to the external circuit, and into the counter electrode where they participate in reduction reactions [3]. The complementary photogenerated holes participate in oxidation reactions at the photoanode-electrolyte interface.

The efficiency of these systems strongly depends on the transportation of photogenerated charge carriers to the back electrode or electrolyte interface prior to charge recombination. The charge carrier lifetime of the semiconductor is a major obstacle for these systems as the involved reactions occur on significantly longer timescales than charge trapping and recombination [4]. Trapping often takes place in electronic defect states which are associated with structural defects, surface imperfections, and impurities. [5] These trap states can capture photogenerated electrons, limiting the photocarrier lifetime and decreasing the population of conduction-band charge carriers [6].

Consequently, the occupancy and energetics of trap states play an important role in determining the availability of mobile charge carriers and the overall charge-transfer efficiency of PEC systems. The occupancy of these states can be controlled in an electrochemical cell using a potentiostat. The cell chamber is filled with an electrolyte that enables electrochemical charge transfer and ensures overall charge neutrality in the cell. An external bias controlled with respect to a reference electrode (for example Ag/AgCl) establishes the electrochemical potential, and therefore the Fermi level in the working electrode. The Fermi level directly defines the occupation of electronic states, including trap states, in the semiconductor [7] [8] [9]. Fermi level control therefore provides an opportunity to investigate the relationship between trap state occupancy and charge transport under electrochemical operating conditions. In particular, understanding the potential-dependent transition of electrons from localized trap states to the conduction band under operating conditions is important for determining how defect states influence the performance of metal-oxide photoelectrodes.

Established spectroelectochemistry (SEC) techniques monitor the visible spectrum under applied electrochemical bias. The bias drives redox reactions in bound molecules which in turn changes their optical absorbance. Monitoring the spectral transmission with respect to the applied voltage provides an excellent method for identifying redox active species and determining the energy needed to add or remove electrons to or from bound states. However, the visible probe cannot provide any insight into free charges that do not exhibit visible transitions. In particular, these measurements are insufficient to quantify the contribution of occupied states to electrical conductivity. Terahertz time domain spectroscopy (THz-TDS) has been used to directly measure the complex conductivity and photoconductivity in several material systems [6] [10] [11]. Combining THz-TDS with potential control therefore provides a complementary

approach which enables the direct measurement of conductivity changes in a material under operating conditions and/or resulting from an applied bias.

THz-SEC is underdeveloped due to difficulties associated with the construction of a THz transparent electrochemical cell. Both the conductive electrodes and the aqueous electrolyte strongly absorb THz radiation, therefore a unique cell design is required. The first THz transparent cell was published in 2018 [7]. The cell design was single use, and could not be disassembled. Another iteration of the concept was demonstrated in 2022. The authors used a spin-coated polymer to bridge the gap between two gold electrodes. The electrodes were short circuited to prevent inhomogeneity in channel doping, and the bias applied to the polymer was referenced to Ag/AgCl [12]. Here, we present a reusable cell design which facilitates modular assembly and disassembly and therefore the comparison of different material systems in identical electrochemical environments. Furthermore, our approach uses a conventional three-electrode cell configuration in which the metal-oxide semiconductor serves directly as the working electrode, with a spatially separated counter electrode demonstrating a true, functioning photoelectrochemical cell. This configuration facilitates insight into the relationship between electrochemical state occupation and charge transport in semiconductor photoanodes.

To demonstrate our newly developed technique we chose wide-bandgap semiconductors TiO_2 and SnO_2. TiO_2 and SnO_2 are commercially available materials often used in photoelectrochemical cells [1] due to their high chemical stability, favorable energy alignment, and charge transport properties. We present a comparison of THz-SEC measurements of SnO_2 and TiO_2, and a method for extracting the quantitative change in conductivity in the material resulting from an applied bias. This represents the first example of conductivity analysis for THz transmission measurements through a layer stack involving electrolyte, semiconductor, and electrode under applied bias, providing a unique characterization of charge transport under fuel cell operating conditions. We also demonstrate that conduction band electron density can be extracted which directly quantifies the density of traps and their relative energy. This technique will provide crucial insight into a range of emerging materials in which defects and traps limit their suitability for commercial applications.

2 Methods

2.1 Electrochemical cell

The electrochemical cell consists of three parts, shown in Figure 1 in their disassembled cross-section. The first component of the cell is machined PTFE, pictured in Figure 1b. The 127 micron recession surrounding the probed region creates the electrolyte window. This is sufficiently thin to minimize THz attenuation by the electrolyte. Solvent channels allow for continuous electrolyte flow through the cell. Electrode probes contact the electrode plate (Figure 1c) at the indicated locations, outside the electrolyte window. A leakless Ag/AgCl reference electrode (eDAQ ET072) is held close to the working electrode region. A quartz window is used in the probed region to provide optical transparency on both sides of the cell, therefore enabling THz-SEC, UV-Vis

SEC, and optical-pump THz-probe (OPTP) measurements in the same cell. The second component is the electrode plate, pictured in Figure 1c. The blue and red regions represent the working and counter electrode contact area, respectively. The pink region is a 5.85 mm x 5.85 mm wire-grid pattern of fluorine-doped tin oxide (FTO) on quartz, fabricated similarly to the method described by Nemes et al. [8]. FTO is an optically transparent, electrically conductive material widely used in optoelectronics, solar cells, and electrochemical applications. A microscope image of the wire-grid region is shown in Figure 1d. The wires are 12 microns with 8 micron gaps between them, facilitating THz transmission through the probed region while maintaining electrical conductivity. The third component is a back plate which screws into the PTFE component (b), holding the electrode plate (c) in place. This cell design allows for simple modular assembly and disassembly such that each sample is measured in an identical cell environment. It also improves upon other thin-cell designs which use a thin Teflon spacer to create the electrolyte window [13] by minimizing the number of components in a simplified design.

2.2 Nanoparticle Pastes

The presented research used three nanoparticular materials, namely a commercial anatase TiO_2 paste (Solaronix Ti-Nanoxide T/SP), with a specified particle size of 15-20 nm compared with anatase TiO_2 and SnO_2 pastes prepared in-house following a modified version of the procedure developed by Antoniuk-Pablant et al. [14] and Ito et al. [15] using commercial nanoparticles (MSE PO7101, SnO_2 and MSE PO2504, TiO_2) with a specified particle size of 50 nm. Briefly, the nanoparticles are combined with ethyl cellulose and α-Terpineol in ethanol using an ultrasonic horn, then the ethanol is evaporated leaving a viscous paste. The paste was then doctor-bladed on the fabricated electrodes. The resulting film was heated from room temperature to 470°C at a rate of 3°C/min., then held at 470°C for 10 minutes to cure. The cured film had a thickness of 4-6 μm, measured via mechanical profilometry.

This fabrication technique is flexible and versatile. Pastes using ethyl cellulose as a binder and terpineol as an organic solvent have been used for WO_3 [16], conductive ceramics [17], nickel [18], NiCuZn ferrite [19], and more [20] [21] [22]. We are therefore confident that this technique can be extended to a wide range of materials, elucidating bias-dependent dynamics that influence their efficiency in fuel cells.

3 Results and Discussion

3.1 THz Cyclic Voltammetry

Cyclic voltammetry, a common technique in electrochemistry, uses a potentiostat to sweep a range of potentials applied to the working electrode (with respect to the reference electrode) in the forward and backward directions. The resulting current between the working and counter electrodes is measured, and the shape of the current vs. potential plot provides information about the reaction [23]. Our new cell design allowed us to combine this established technique with a simultaneous measurement of the THz transmission. The resulting THz transmission versus applied voltage traces

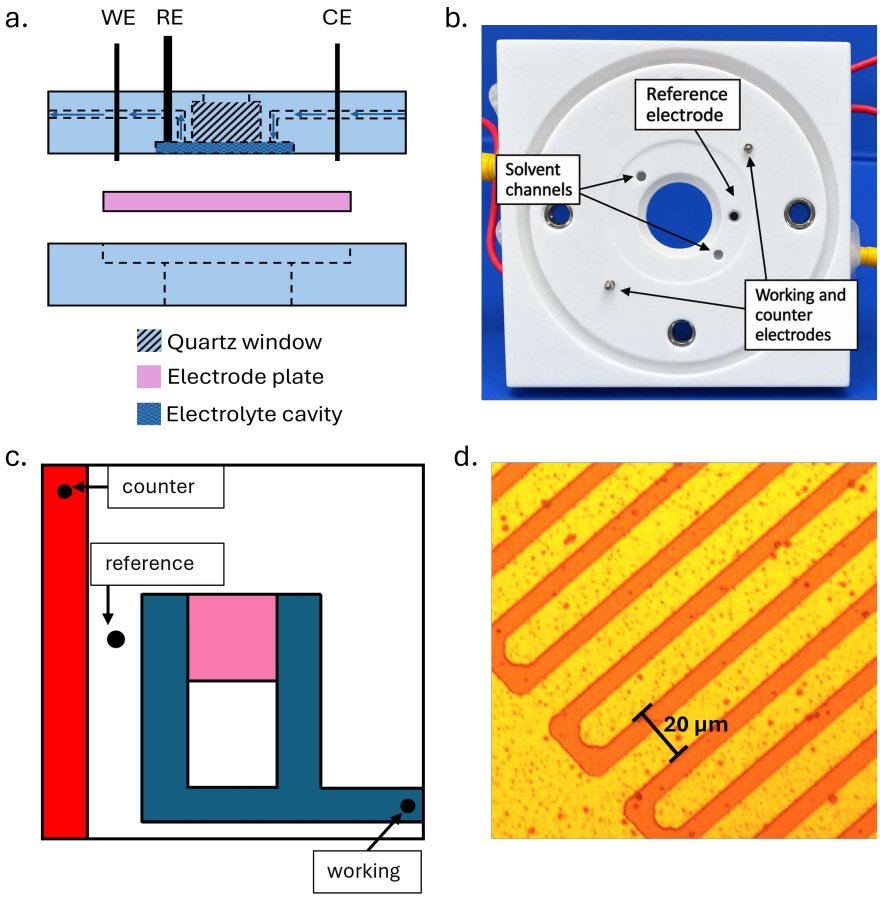

Fig. 1 Components of the novel THz electrochemical cell design. a) Side view of the disassembled three-component electrochemical cell, including the front plate (top) with solvent channels, electrolyte window, and electrode probes, electrode plate (middle), and back plate (bottom). b) Front plate of the electrochemical cell. c) Electrode plate, with solid FTO counter electrode and working electrode contact areas in red and blue, respectively, and wire-grid FTO working electrode region in pink. d) Microscope image of the wire-grid working electrode.

are called THz cyclic voltammetry (TCV). A representative measurement for SnO_2 is presented in Figure 2a, where the THz transmission is reported as a percent change with respect to the time-domain amplitude of transmission at the starting potential.

The scan begins with the potential set to 0.2 V versus an Ag/AgCl reference electrode [24]. The potential is swept in the negative direction down to -1.2 V, then back to the starting potential. A negative bias raises the Fermi level of electrons in the semiconductor [8] [9]. As shown in the inset of Figure 2a, the CV-measured current onset occurs immediately with the change in potential. In contrast, the TCV measured THz transmission is constant until the potential reaches approximately -0.25 V. The decreased THz transmission indicates the presence of mobile electrons in the conduction band, as mobile electrons reflect and absorb THz radiation [10] [11]. A

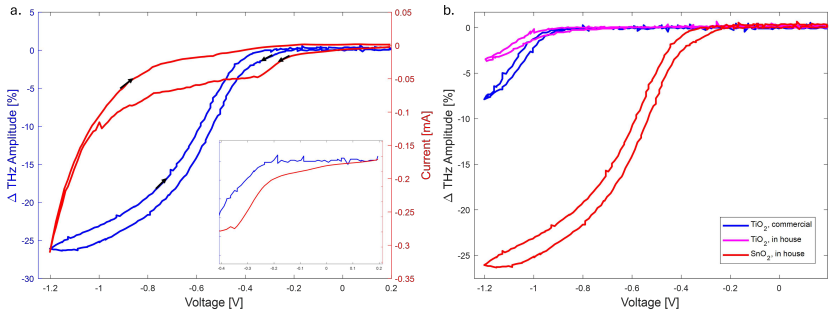

Fig. 2 a.) THz cyclic voltammetry measurement of SnO_2. The inset shows that the onset of current occurs immediately with the change in potential, while the THz transmission is constant until -0.25 V. b.) THz cyclic voltammetry of commercial TiO_2 paste, and in-house synthesized TiO_2 and SnO_2 pastes. The onset of conductivity in both TiO_2 pastes occurs at bias more negative than -0.9 V, compared to -0.25 V for SnO_2.

bias of +0.2V to -0.25 V is insufficient to populate the conduction band, thus the TCV traces are unchanged, while the bias still drives a current into the sample cell as measured with CV. This clearly demonstrates that TCV is sensitive to mobile states, while CV monitors overall charge transfer within the cell. The combined measurement therefore provides an in-depth insight into the underlying physics in emerging semiconductive materials. The onset of conductance at -0.25V cannot be caused by electrons excited across the wide (3.6 eV) bandgap of SnO_2 [25], therefore the decrease in THz transmission must be associated with trap state ionization.

Repeated TCV measurements of this material system reveal that the magnitude of the current (the parameter measured in conventional CV) varies between samples, while the change in THz transmission is reproducible across multiple samples. This is because the current is proportional to the surface area of the electrode [26], and the electrode fabrication and doctor blading of the paste result in some inconsistencies in the surface area. While the current is a measurement of the properties of the full electrochemical system, the THz transmission is related only to the properties of the semiconductor at the working electrode, in the $\approx$ 4mm THz focal spot. Our fabrication ensures sample to sample reproducibility over this smaller area, which is easier to achieve. Thus TCV and THz-SEC can be more readily applied to challenging materials. Our results demonstrate that TCV is a complementary technique which provides unique access to the energetics of trap states in metal-oxide semiconductors and directly distinguishes between bound and mobile charges: an undercharacterized aspect of electrochemical systems.

Previous electrochemical studies demonstrated that changes in electrolyte concentration can modify the electrical double-layer, influencing the relationship between applied potential and charge accumulation at the electrode surface [27]. We therefore verified the impact of the electrolyte concentration on our newly established TCV technique. We observed a minor influence, with higher electrolyte concentration resulting in a stronger THz attenuation at the same applied bias (see SI). So long as the concentration is sufficiently high to overcome the uncompensated resistance associated with the thin-cell geometry, this effect is minor, and the interpretation of the

results is unchanged. We therefore suggest that future studies should perform control measurements to identify the minimum electrolyte concentration required for accurate measurements.

The versatility of our new technique is demonstrated by performing additional TCV measurements using films made from commercial and in-house fabricated TiO_2 pastes. A comparison between the three metal-oxide semiconductor pastes is given in Figure 2b. The onset of conductivity in the TiO_2 pastes does not occur until biases less than -0.9 V. Knowing that a more negative applied bias is needed to promote electrons into the conduction band, we can conclude that the TiO_2 paste has a smaller density of trap states close to the conduction band as compared to SnO_2. It is interesting that the commercial (15-20 nm) and in-house (50 nm) TiO_2 pastes exhibit similar TCV dynamics. Prior research showed that the density of deep electron traps in TiO_2 is dependent on nanoparticle size, with smaller nanoparticles having a higher density of deep electron traps [28]. The past studies relied on transient absorption measurements, and therefore could not distinguish shallow trap-state electrons from mobile, conduction band carriers. We use THz-SEC to access these shallow trap states, and see that the onset of conductivity occurs around the same electrochemical potential for both pastes, with the smaller nanoparticles of the commercial paste exhibiting a larger conductivity response. This result indicates that the shallow trap states in the two TiO_2 pastes have similar energies but different occupancy, and demonstrates that TCV provides a better trap-state sensitivity compared to established optical techniques. We cannot, however, relate the difference in THz attenuation solely to nanoparticle size, as the fabrication and synthesis techniques used for the nanoparticles and paste also influence defect and trap state density.

3.2 Static Potential Measurements

Dynamic TCV utilizes the time-domain amplitude to determine the potentials at which trap states are ionized into the conduction band. We extend the TCV technique to measure the full THz-TDS trace under a static applied bias, called bias resolved THz spectroscopy (BRTS). BRTS allows us to examine the spectral response of the material under applied bias in an electrochemical environment. As shown in Figure 3, a broadband decrease in THz transmission consistent with the presence of mobile electrons [29] is observed in SnO_2, verifying that the decreased THz transmission is related to conductivity rather than changes to the lattice.

The bias-induced change in conductivity can be calculated from the transfer function defined by Equation 1, where the Fourier-transformed THz transmission through the cell under applied bias is divided by that through the cell at 0 V, similar to the method used to describe photoconductivity.

$$T(\omega) = \frac{E_{biased}(\omega)}{E_{0V}(\omega)} \tag{1}$$

The THz amplitude measured in BRTS is defined by interface transmission (t_{ij}), layer propagation (P_j), and reflective Fabry-Perot etalon (FP_{ijk}) terms analogous to the terms used and defined for time-resolved THz spectroscopy (TRTS) in previous

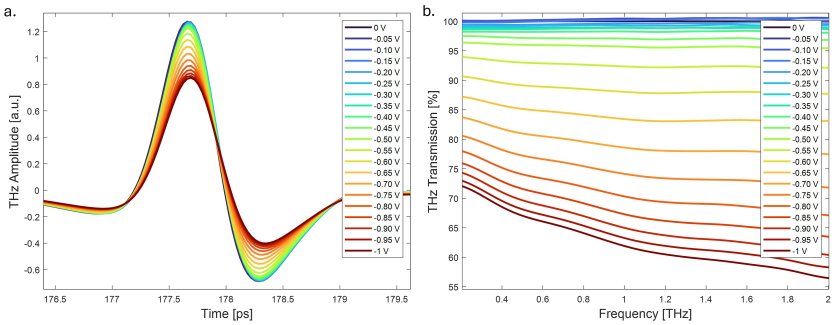

Fig. 3 a.) THz-TDS measurements of SnO_2. b.) Fourier-transformed THz transmission spectra given as a percentage of the transmission under the 0 V bias condition.

publications [6] [10] [30] [31], and illustrated for the electrochemical cell by Figure 4 (not to scale).

$$\tilde{E}_T = \tilde{t}_{01}\tilde{P}_1\tilde{t}_{12}\tilde{P}_2\tilde{t}_{23}\tilde{P}_3\tilde{t}_{34}\tilde{P}_4\tilde{t}_{40}\tilde{FP}_{012}\tilde{FP}_{123}\tilde{FP}_{234}\tilde{FP}_{340}\tilde{E}_I$$

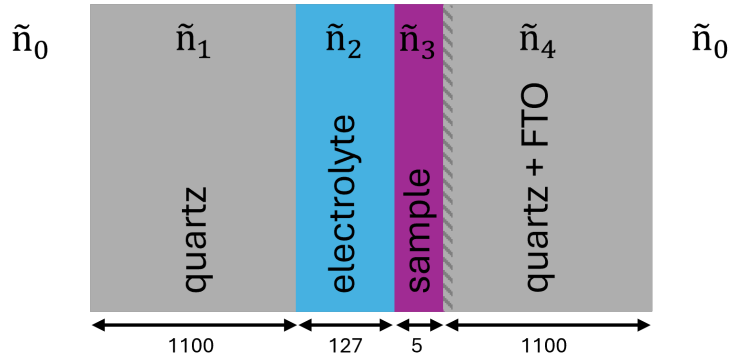

Fig. 4 Representation of the layers and refractive indices involved in the transfer function for the electrochemical cell. Terms which remain in the BRTS analysis are colored purple. Layer thicknesses are given in microns. This figure is not drawn to scale.

Most of the terms in the equation shown in Figure 4 do not change under applied bias, simplifying the extraction of the bias-induced change to terms related to the sample layer and its interfaces. This includes the transmission from electrolyte to semiconductor t_{23}, propagation through the semiconductor P_3, transmission from semiconductor to electrode plate t_{34}, and Fabry-Perot etalons within the electrolyte FP_{123}, semiconductor FP_{234}, and electrode plate FP_{340}.

Similar to TRTS data processing, we chose to avoid the thin-film approximation to ensure that our results can be generalized to even thicker layers [32]. This resulted in more computational complexity and required us to establish a numerical model for the transfer function [30]. We exclude the FP_{340} term, as these reflections are

caused in the 1,100 μm thick quartz substrates and therefore arrive outside of the measured time window of 12 ps following the primary transmitted pulse. The FP_{123} term is terminated after the second element, as the transmission through an aqueous electrolyte is very low and after multiple round trips will contribute only a fraction of a percent to the measured signal. Because the sample material is very thin (4-6 micrometers as measured with mechanical profilometry), we assume that an infinite number of reflections appear in the measured time window and thus use the infinite sum expression to describe the final Fabry-Perot term FP_{234} [6] [30]. With these simplifications the modeled change in transmission is described as:

$$T_{model} = \frac{E_{biased}}{E_{0V}} = \frac{t_{23^*}P_{3^*}t_{3^*4}FP_{123^*}FP_{23^*4}}{t_{23}P_3t_{34}FP_{123}FP_{234}} \triangleq T_{measured} \tag{2}$$

where the asterisk denotes the biased sample.

The only unknown in the equation above is the complex refractive index of the biased sample, n_{3^*}. Using numerical optimization, we find the complex value of n_{3^*} that minimizes the difference between the modeled and measured transfer functions at each frequency point. The optimization criteria is given by Equations 3-5 [33].

$$\delta = (\delta\rho)^2 + (\delta\phi)^2 \tag{3}$$

where

$$\delta\rho = \ln|T_{model}(\omega)| - \ln|T_{measured}(\omega)| \tag{4}$$

and

$$\delta\phi = \arg(T_{model}(\omega)) - \arg(T_{measured}(\omega)) \tag{5}$$

So far this optimization did not invoke any models or assumptions, except the known thickness and refractive index of the materials used in the cell. To extract the conductivity from the refractive index change $\Delta n = n_{biased} - n_{unbiased}$ we now assume that the lattice permittivity remains constant under applied bias and calculate the change in conductivity as:

$$\Delta\sigma(\omega) = -\mathrm{i}(\Delta n)^2\omega\varepsilon_0 \tag{6}$$

analogous to the method used to calculate TRTS-photoconductivity [6]. The real part of the calculated change in conductivity is shown in Figure 5 (see SI for imaginary part).

The change in conductivity is minimal for biases more positive than -0.6 V. When the potential becomes more negative a monotonic increase in conductivity is observed, reaching 1,000 S/m at 1.2 THz for a bias of -1 V. This result establishes BRTS as a novel technique to understand conductivity in emerging materials under fuel cell operating conditions.

In contrast to the more familiar photoconductivity measured via TRTS, the BRTS conductivity is related to ionized trap states rather than carriers excited across the bandgap. The wide bandgap of SnO_2 requires an optical pump wavelength of 267 nm (4.6 eV) for direct measurements of the semiconductor's THz photoconductivity dynamics [4]. Due to the large bandgap many OPTP measurements of SnO_2 and TiO_2 use dye-sensitized systems operating at longer pump-wavelengths more relevant for solar applications [34] [5] [35] [36].

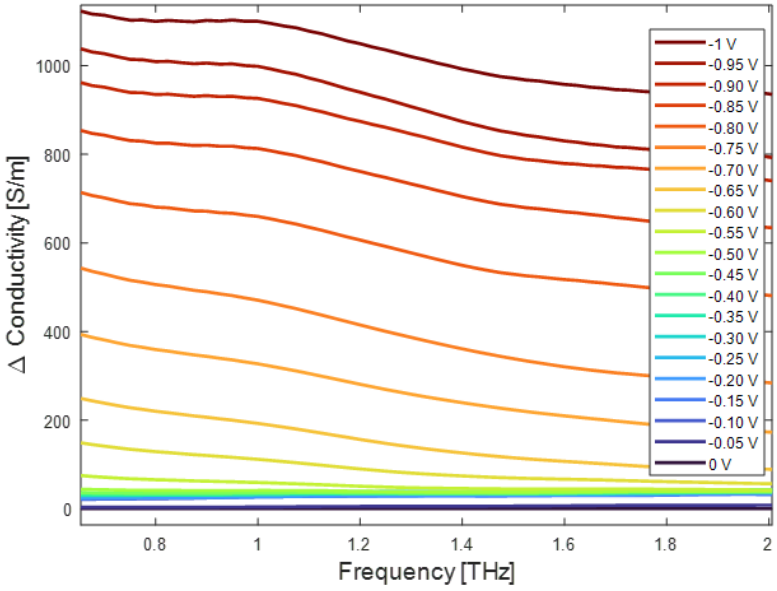

Fig. 5 Real part of the change in frequency-dependent complex conductivity of SnO_2 for each applied bias condition, from 0V to -1V.

We further explore the bias-induced conductivity dynamics by fitting the data with the Drude-Smith model:

$$\Delta\sigma(\omega) = \frac{ne^2\tau}{m^*}\frac{1}{1-i\omega\tau}(1+\frac{c}{1-i\omega\tau}) \tag{7}$$

where the carrier density N, scattering time τ, and backscattering parameter c are used as fit parameters. We use the established effective mass in SnO_2 of $m^* = 0.275m_e$ [37]. The complex conductivity spectra for biases from -0.5 V to -1 V are globally fit, so that all conductivity changes are attributed to a change in the carrier density N. The scattering time extracted from the fit model is $\tau = 54$ fs, in excellent agreement with TRTS results on similar SnO_2 nanoparticles.[4] In contrast to the previous TRTS work, the backscattering parameter extracted from BRTS is near $c = 0$, while TRTS results typically give a value between $c = -0.5$ to $c = -0.9$ [4] [5]. The larger influence of backscattering on the photoconductivity could be related to the electron's excess energy provided by the above bandgap excitation, or it could be related to differences in the material. Our study used 50 nm SnO_2 nanoparticles, more than twice the diameter used in previous studies [4]. The directional backscattering described with the c-parameter is directly related to the finite size of the nanoparticle, therefore carriers in a larger nanoparticle can be expected to experience less backscattering.

The bias-dependent carrier densities (N) are presented in Figure 6a. The extracted carrier density increases with increasingly negative applied bias, from $0.06 \times 10^{17} cm^{-3}$

at -0.5 V to $2.20 \times 10^{17} cm^{-3}$ at -1 V. This approximately 33-fold increase is consistent with the progressive filling of conduction band states associated with trap state ionization.

The rate of charge carrier accumulation can be determined by taking the derivative of the carrier density with respect to applied bias, shown in Figure 6b. We see that the highest rate of accumulation occurs at an electrochemical potential of -0.75 V. This indicates the range in which the charge carrier population is most sensitive to changes in electrochemcial potential.

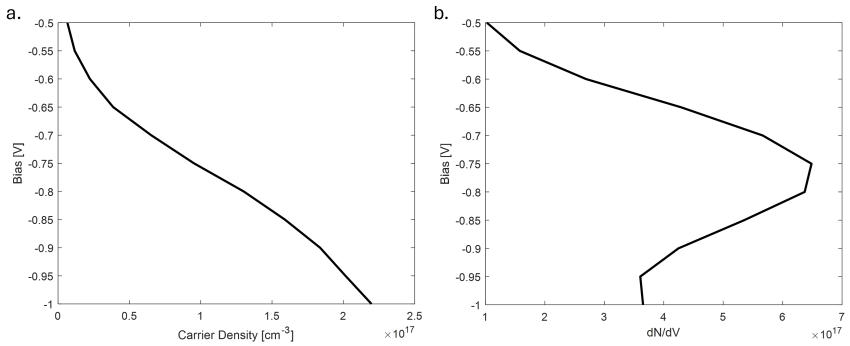

Fig. 6 a.) The carrier density N extracted from the Drude-Smith fit at each electrochemical bias condition. b.) The derivative of N with respect to applied bias at each bias condition, revealing the rate of carrier accumulation.

Importantly, these results demonstrate that THz-SEC can be used to quantify changes in charge carrier populations introduced in an electrochemical environment (TCV), as well as identifying frequency-dependent properties and dynamics of those carriers (BRTS). This establishes THz-SEC as a complementary technique for investigating trap state occupation and energetics as well as charge transport in metal-oxide semiconductors under operating conditions.

4 Conclusion and Outlook

A novel THz and optically transparent electrochemical cell was designed and utilized for both THz cyclic voltammetry (TCV) and bias resolved THz spectroscopy (BRTS) measurements of metal-oxide semiconductors TiO_2 and SnO_2. We demonstrated that THz-SEC provides access to undercharacterized trap state energetics and occupancies which govern the performance of all opto-electronic devices. Bias-induced conductivity values were extracted from the THz-SEC measurements, delivering novel insight into the charge transport properties of metal-oxide photoanodes. We further use Drude-Smith fitting of the BRTS traces to extract bias-induced conductivities to elucidate the carrier density as a function of applied bias, revealing the relationship between electrochemical energy and charge carrier accumulation.

The combined optical and THz transparency of the cell provides a pathway for a number of research avenues. Future research will focus on the relationship between

applied bias and charge carrier lifetime under optical excitation for hybrid and dye-sensitized systems.

Declarations

The authors declare no competing interests.

Supplementary information. Supplementary Information can be found at:

Acknowledgements. This material is based upon work supported by the Air Force Office of Scientific Research under Award No. FA9550-23-1-0630 and UNT Seed grant RSG-2026-007. We would like to thank Mark Lanier and Tracy Lynch from the Physics Machine Shop for machining the many versions of the electrochemical cell. We would furthermore like to thank Vanessa Bristol and Danil Khaiumov for their help with CST simulations of the patterned electrode.

References

[1] Grätzel, M.: Photoelectrochemical cells. Nature **414**(6861), 338–344 (2001) https://doi.org/10.1038/35104607

[2] Chiu, Y.-H., Lai, T.-H., Kuo, M.-Y., Hsieh, P.-Y., Hsu, Y.-J.: Photoelectrochemical cells for solar hydrogen production: Challenges and opportunities. APL Materials **7**(8) (2019) https://doi.org/10.1063/1.5109785

[3] Song, K., Liu, H., Chen, B., Gong, C., Ding, J., Wang, T., Liu, E., Ma, L., Zhao, N., He, F.: Toward efficient utilization of photogenerated charge carriers in photoelectrochemical systems: Engineering strategies from the atomic level to configuration. Chemical Reviews **124**(24), 13660–13680 (2024) https://doi.org/10.1021/acs.chemrev.4c00382

[4] Regan, K.P., Swierk, J.R., Neu, J., Schmuttenmaer, C.A.: Frequency-dependent terahertz transient photoconductivity of mesoporous sno_2 films. The Journal of Physical Chemistry C **121**(29), 15949–15956 (2017) https://doi.org/10.1021/acs.jpcc.7b02318

[5] Neu, J., Ostresh, S., Regan, K.P., Spies, J.A., Schmuttenmaer, C.A.: Influence of dye sensitizers on charge dynamics in sno_2 nanoparticles probed with thz spectroscopy. J. Phys. Chem. C **124**(6), 3482–3488 (2020) https://doi.org/10.1021/acs.jpcc.9b11024

[6] Neu, J.: Optical pump terahertz probe (optp) and time resolved terahertz spectroscopy (trts) of emerging solar materials. APL Photonics **8**(7) (2023) https://doi.org/10.1063/5.0152726

[7] Nemes, C.T., Swierk, J.R., Schmuttenmaer, C.A.: A terahertz-transparent electrochemical cell for in situ terahertz spectroelectrochemistry. Analytical Chemistry **90**(7), 4389–4396 (2018) https://doi.org/10.1021/acs.analchem.7b04204

[8] Nemes, C.T., Koenigsmann, C., Schmuttenmaer, C.A.: Functioning photoelectrochemical devices studied with time-resolved terahertz spectroscopy. The Journal of Physical Chemistry Letters **6**(16), 3257–3262 (2015) https://doi.org/10.1021/acs.jpclett.5b01473

[9] Tachibana, Y., Haque, S.A., Mercer, I.P., Moser, J.E., Klug, D.R., Durrant, J.R.: Modulation of the rate of electron injection in dye-sensitized nanocrystalline tio$_2$ films by externally applied bias. The Journal of Physical Chemistry B **105**(31), 7424–7431 (2001) https://doi.org/10.1021/jp010173q

[10] Neu, J., Schmuttenmaer, C.A.: Tutorial: An introduction to terahertz time domain spectroscopy (thz-tds). Journal of Applied Physics **124**(23) (2018) https://doi.org/10.1063/1.5047659

[11] Hamilton, K., Neu, J.: Terahertz spectroscopy of mofs reveals dynamic structure and contact free ultrafast photoconductivity. APL Materials **12**(1) (2024) https://doi.org/10.1063/5.0179574

[12] Tsokkou, D., Cavassin, P., Rebetez, G., Banerji, N.: Bipolarons rule the short-range terahertz conductivity in electrochemically doped p3ht. Materials Horizons **9**(1), 482–491 (2022) https://doi.org/10.1039/d1mh01343b

[13] Machan, C.W., Sampson, M.D., Chabolla, S.A., Dang, T., Kubiak, C.P.: Developing a mechanistic understanding of molecular electrocatalysts for co$_2$ reduction using infrared spectroelectrochemistry. Organometallics **33**(18), 4550–4559 (2014) https://doi.org/10.1021/om500044a

[14] Antoniuk-Pablant, A., Terazono, Y., Brennan, B.J., Sherman, B.D., Megiatto, J.D., Brudvig, G.W., Moore, A.L., Moore, T.A., Gust, D.: A new method for the synthesis of β-cyano substituted porphyrins and their use as sensitizers in photoelectrochemical devices. Journal of Materials Chemistry A **4**(8), 2976–2985 (2016) https://doi.org/10.1039/c5ta07226c

[15] Ito, S., Chen, P., Comte, P., Nazeeruddin, M.K., Liska, P., Péchy, P., Grätzel, M.: Fabrication of screen-printing pastes from tio$_2$ powders for dye-sensitised solar cells. Progress in Photovoltaics: Research and Applications **15**(7), 603–612 (2007) https://doi.org/10.1002/pip.768

[16] Thirumalaisamy, L., Wei, Z., Davies, K.R., Allan, M.G., McGettrick, J., Watson, T., Kuehnel, M.F., Pitchaimuthu, S.: Dual shield: Bifurcated coating analysis of multilayered wo $_3$ /bivo $_4$ /tio $_2$ /niooh photoanodes for sustainable solar-to-hydrogen generation from challenging waters. ACS Sustainable Chemistry &; Engineering **12**(8), 3044–3060 (2024) https://doi.org/10.1021/acssuschemeng.3c06528

[17] Murakami, S., Ri, K., Itoh, T., Izu, N., Shin, W., Inukai, K., Takahashi, Y., Ando,

Y.: Effects of ethyl cellulose polymers on rheological properties of (la,sr)(ti,fe)o3-terpineol pastes for screen printing. Ceramics International **40**(1), 1661–1666 (2014) https://doi.org/10.1016/j.ceramint.2013.07.057

[18] Lee, S., Paik, U., Yoon, S., Choi, J.: Dispersant-ethyl cellulose binder interactions at the ni particle-dihydroterpineol interface. Journal of the American Ceramic Society **89**(10), 3050–3055 (2006) https://doi.org/10.1111/j.1551-2916.2006.01192.x

[19] Hsu, C.-J., Jean, J.-H.: Formulation and dispersion of nicuzn ferrite paste. Materials Chemistry and Physics **78**(2), 323–329 (2003) https://doi.org/10.1016/s0254-0584(01)00590-9

[20] Zhang, Y., Huang, X., Lu, Z., Liu, Z., Ge, X., Xu, J., Xin, X., Sha, X., Su, W.: A screen-printed ce0.8sm0.2o1.9 film solid oxide fuel cell with a ba0.5sr0.5co0.8fe0.2o3-δ cathode. Journal of Power Sources **160**(2), 1217–1220 (2006) https://doi.org/10.1016/j.jpowsour.2006.02.048

[21] Phair, J.W.: Rheological analysis of concentrated zirconia pastes with ethyl cellulose for screen printing sofc electrolyte films. Journal of the American Ceramic Society **91**(7), 2130–2137 (2008) https://doi.org/10.1111/j.1551-2916.2008.02443.x

[22] SHIN, W., NISHIBORI, M., OHASHI, M., IZU, N., ITOH, T., MATSUBARA, I.: Ceramic catalyst combustors of pt-loaded-alumina on microdevices. Journal of the Ceramic Society of Japan **117**(1365), 659–665 (2009) https://doi.org/10.2109/jcersj2.117.659

[23] Bard, A.J.: Electrochemical Methods, 2. edition edn. Wiley, New York (2001). Literaturangaben

[24] Elgrishi, N., Rountree, K.J., McCarthy, B.D., Rountree, E.S., Eisenhart, T.T., Dempsey, J.L.: A practical beginner's guide to cyclic voltammetry. J. Chem. Educ. **95**(2), 197–206 (2018) https://doi.org/10.1021/acs.jchemed.7b00361

[25] Buniyamin, I., Eswar, K.A., Idorus, M.Y., Othman, Z., Rostan, N.F., Mohammad, M., Shamsudin, M.S., Tukimon, M.A., Rahman, A.F.M.M., Malek, M.F.: Tuning crystallinity and band gap of sno2 nanoparticles through green synthesis and controlled calcination. Sustainable Chemistry One World **11**, 100259 (2026) https://doi.org/10.1016/j.scowo.2026.100259

[26] Kissinger, P.T., Bott, A.W.: Electrochemistry for the non-electrochemist. Current Separations **20**(2), 51–53 (2002)

[27] Zhang, Z., Huang, J.: Microstructure of electrical double layers at highly charged states. JACS Au **5**(7), 3453–3467 (2025) https://doi.org/10.1021/jacsau.5c00508

[28] Naniwa, S., Kato, K., Yamamoto, A., Yoshida, H., Yamakata, A.: Particle size dependent trap states of photoexcited carriers in anatase tio $_2$ nanoparticles. The Journal of Physical Chemistry C **127**(8), 4295–4302 (2023) https://doi.org/10.1021/acs.jpcc.2c08125

[29] Beard, M.C., Turner, G.M., Schmuttenmaer, C.A.: Transient photoconductivity in gaas as measured by time-resolved terahertz spectroscopy. Physical Review B **62**(23), 15764–15777 (2000) https://doi.org/10.1103/physrevb.62.15764

[30] Tayvah, U., Spies, J.A., Neu, J., Schmuttenmaer, C.A.: Nelly: A user-friendly and open-source implementation of tree-based complex refractive index analysis for terahertz spectroscopy. Analytical Chemistry **93**(32), 11243–11250 (2021) https://doi.org/10.1021/acs.analchem.1c02132

[31] Lee, Y.-S. (ed.): Principles of Terahertz Science and Technology. SpringerLink. Springer, Boston, MA (2009). Includes bibliographical references and index

[32] Neu, J., Regan, K., Swierk, J.R., Schmuttenmaer, C.A.: Applicability of the Thin-film Approximation in Terahertz Photoconductivity Measurements. Appl. Phys. Lett. **113**(22), 233901 (2018) https://doi.org/10.1063/1.5052232

[33] Duvillaret, L., Garet, F., Coutaz, J.-L.: A reliable method for extraction of material parameters in terahertz time-domain spectroscopy. IEEE Journal of Selected Topics in Quantum Electronics **2**(3), 739–746 (1996) https://doi.org/10.1109/2944.571775

[34] Tiwana, P., Docampo, P., Johnston, M.B., Snaith, H.J., Herz, L.M.: Electron mobility and injection dynamics in mesoporous zno, sno $_2$, and tio $_2$ films used in dye-sensitized solar cells. ACS Nano **5**(6), 5158–5166 (2011) https://doi.org/10.1021/nn201243y

[35] Jayworth, J.A., Decavoli, C., Capobianco, M.D., Menzel, J.P., Adler, S.R., Kocoj, C.A., Freeze, J.G., Crabtree, R.H., Guo, P., Batista, V.S., Brudvig, G.W.: Bodipy chemisorbed on sno_2 and tio_2 surfaces for photoelectrochemical applications. ACS Applied Materials and Interfaces **16**(12), 14841–14851 (2024) https://doi.org/10.1021/acsami.3c18827

[36] Lee, S.H., Regan, K.P., Hedström, S., Matula, A.J., Chaudhuri, S., Crabtree, R.H., Batista, V.S., Schmuttenmaer, C.A., Brudvig, G.W.: Linker length-dependent electron-injection dynamics of trimesitylporphyrins on sno_2 films. The Journal of Physical Chemistry C **121**(41), 22690–22699 (2017) https://doi.org/10.1021/acs.jpcc.7b07855

[37] Button, K.J., Fonstad, C.G., Dreybrodt, W.: Determination of the electron masses in stannic oxide by submillimeter cyclotron resonance. Physical Review B **4**(12), 4539–4542 (1971) https://doi.org/10.1103/physrevb.4.4539

Supplementary Files

This is a list of supplementary files associated with this preprint. Click to download.

- SI.pdf